Results in Physics 29 (2021) 104728

Contents lists available at ScienceDirect

Results in Physics

journal homepage: www.elsevier.com/locate/rinp

Measurement of the quantum defects of ^{85}Rb *P* and *F*-series via microwave-assisted electromagnetically induced transparency spectroscopy

Shaohua Li [a,b], Jinpeng Yuan [a,b,*], Lirong Wang [a,b,*], Liantuan Xiao [a,b], Suotang Jia [a,b]

[a] State Key Laboratory of Quantum Optics and Quantum Optics Devices, Institute of Laser Spectroscopy, Shanxi University, 92 Wucheng Road, Taiyuan 030006, China
[b] Collaborative Innovation Center of Extreme Optics, Shanxi University, 92 Wucheng Road, Taiyuan 030006, China

ARTICLE INFO

Keywords:
Microwave-assisted EIT spectroscopy
Resonant transition frequency
Quantum defect

ABSTRACT

We report the measurement of the quantum defects of ^{85}Rb $P_{3/2}$ and $F_{7/2}$-series Rydberg levels in a room temperature vapor cell by microwave-assisted electromagnetically induced transparency (EIT) spectroscopy. First, a novel microwave optical three-photon excitation method is employed to obtain the microwave-assisted EIT spectroscopy of the $5S_{1/2} - 5P_{3/2} - nD_{5/2} - (n+1)P_{3/2}$ or $(n\text{-}1)F_{7/2}$ transition. Next, the Stark shifts of the corresponding Rydberg states relative to the Rabi frequency of microwave field are measured with high accuracy. Finally, the quantum defects, $\delta_0 = 2.64142(15)$, $\delta_2 = 0.295$ for $P_{3/2}$-series, and $\delta_0 = 0.016411(16)$, $\delta_2 = -0.0784$ for $F_{7/2}$-series, are forcibly extracted by the modified Rydberg-Ritz formula. This result can serve as a check on advanced theoretical calculations and promote the application of quantum simulations and quantum sensors in atomic ensembles.

Introduction

Rydberg atoms are the perfect candidates for quantum information processing [1,2], nonlinear quantum optics [3,4,5], and the detection of microwave and terahertz electric fields [6 –9] owing to the remarkable properties of large dipole moments ($\sim$ n^2), long radiative lifetime ($\sim$ n^3), and large polarizability ($\sim$ n^7). In alkali-metal atoms, the deviation from the hydrogen levels due to the interaction between the ionic core of the atom and the valence electron, can be described in terms of quantum defect [10]. Accurate values of quantum defects provide a theoretical basis for predicting the properties of high-lying states for a core of any charge, such as the Stark effect [11], the ionic dipole and the quadrupole polarizabilities [12 –14] of the atoms.

Research on quantum defects of highly excited rubidium Rydberg atoms have attracted considerable attention. The quantum defects of ^{85}Rb atoms have been measured using optical excitation methods, such as single- and multi-step laser excitation spectroscopy [15 –19]. The uncertainties in the results are mainly limited by the accuracy of the wavelength meter, which is often in the magnitude range of tens megahertz. Several high-precision measurement methods have been proposed, such as optical frequency comb calibration [20,21] and microwave excitation spectroscopy [12,22 –26]. However, the wavelength calibration is complicated by the optical frequency combs. But the microwave excitation spectroscopy has a high resolution on the order of kHz. At the same time, the extrapolation method, which provides an estimate of the absolute frequency based on the frequency when the microwave field strength is known, can improve the measurement accuracy by several orders of magnitude [27]. Therefore, a novel experimental method, microwave-assisted EIT spectroscopy combined with Rydberg-series extrapolation, is employed to determine the quantum defects, which can greatly improve the measurement accuracy.

Recently, the ***nP*** and ***nF*** states of Rydberg atoms has been widely studied in recent years for several merits. First, the lack of corresponding excitation lasers of the ***nP*** and ***nF*** states renders the related research challenging to realize, even though it is substantially significant [9,16]. Second, the ***nP*** states are more desirable for the observation of the excitation blockade effect, the pendular “butterfly” Rydberg molecule, and the Rydberg dressing state [28,29]. Third, the ***nF*** states are beneficial for understanding the effects of electric and magnetic field owing to its abundantly hyperfine energy levels [30].

In this work, we measure the quantum defects of the $P_{3/2}$ and $F_{7/2}$-series of ^{85}Rb by microwave-assisted EIT spectroscopy in a room temperature vapor. First, the dependence of the Stark shifts of the corresponding Rydberg states on the Rabi frequency of microwave field are

* Corresponding authors at: State Key Laboratory of Quantum Optics and Quantum Optics Devices, Institute of Laser Spectroscopy, Shanxi University, 92 Wucheng Road, Taiyuan 030006, China.
E-mail addresses: yjp@sxu.edu.cn (J. Yuan), wlr@sxu.edu.cn (L. Wang).

https://doi.org/10.1016/j.rinp.2021.104728
Received 7 June 2021; Received in revised form 5 August 2021; Accepted 19 August 2021
Available online 23 August 2021
2211-3797/

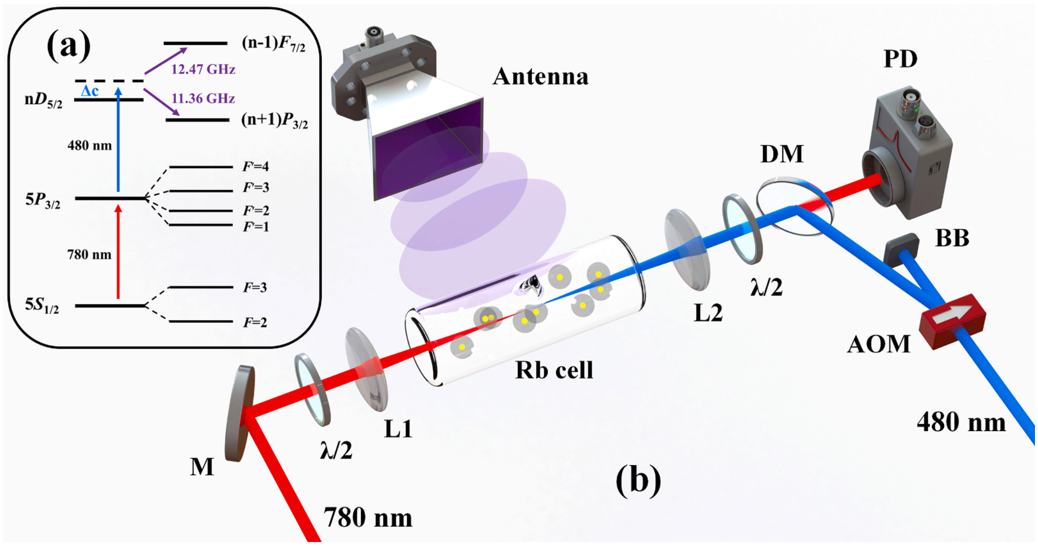

Fig. 1. (a) Energy-level diagram of ^{85}Rb. (b) Experimental setup. BB, beam block; λ/2, half-wave plate; M, mirror; DM, dichroic mirror; L: lens; AOM, acousto-optic modulator; PD: photodiode.

investigated. Second, the resonant transition frequencies of $nD_{5/2}$ – $(n+1)P_{3/2}$ and $(n\text{-}1)F_{7/2}$ (n = 51–57) transitions are obtained by extrapolating the frequency shifts to zero microwave field with high accuracy. Finally, the quantum defects of $P_{3/2}$ and $F_{7/2}$-series are extracted by the modified Rydberg-Ritz formula. This result provides an effective verification of the existing theory and paves the way for studying quantum simulations and quantum sensors in atomic ensembles.

Experimental setup

The atomic energy-level configuration of ^{85}Rb employed in this experiment is shown in Fig. 1(a). A weak probe field (red) excites the atoms from $5S_{1/2}$(F = 3) to $5P_{3/2}$(F′ = 4) hyperfine state, and a strong coupling field (blue) couples the $5P_{3/2}$(F′ = 4) state to the highly excited Rydberg state $nD_{5/2}$. A microwave field covered the adjacent Rydberg transition of $nD_{5/2}$ – $(n+1)P_{3/2}$ (or $(n\text{-}1)F_{7/2}$) is employed to obtain the microwave-assisted EIT spectrum.

The experimental setup is depicted in Fig. 1(b). The probe laser, at the wavelength of 780 nm, is provided by an external cavity diode laser (DL pro, Toptica), and the frequency is locked on the $5S_{1/2}$(F = 3) – $5P_{3/2}$(F′ = 4) transition via saturation absorption spectroscopy (SAS). The coupling laser is provided by a frequency doubled amplified diode laser (DLC TA-SHG pro, Toptica) operating at 480 nm. That beam is split into two beams by a half-wave plate and a polarization beam splitter (PBS). One beam is used to lock the frequency of coupling laser by the EIT spectrum. The other beam enters into a frequency shift system composed by two acousto-optic modulators (AOM) to achieve the adjustable frequency shift, the frequency is monitored by a wavelength meter (WS-7, Highfiness). The intensity modulation is used to improve the signal-to-noise ratio (SNR) of spectrum by introducing a chopper wheel (Stanford Research Systems, SR540) into the optical path with a 1.5 kHz modulation frequency. Then, the beam overlaps with the probe beam in the center of the rubidium vapor cell, which has a length of 100 mm and 25 mm in diameter. The probe beam passing through the vapor cell is detected by a photodiode, and demodulated with a lock-in amplifier (SR830, Stanford Research Systems).

The microwave field, generated by a microwave signal source (SMB100A, Rohde & Schwarz), is emitted from a horn antenna and propagates perpendicularly to the direction of probe and coupling beams. When the microwave field frequency sweeps over the $nD_{5/2}$ to $(n+1)P_{3/2}$(or $(n\text{-}1)F_{7/2}$) transition, the microwave-assisted EIT spectrum can be obtained.

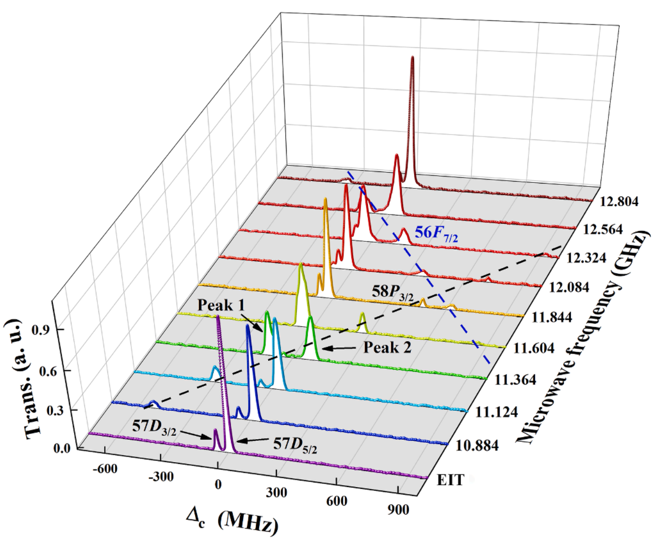

Fig. 2. Microwave-assisted EIT spectra as a function of the coupling laser frequency detuning Δ_c with different microwave field frequencies. The marked peaks (peaks 1 and 2) are the Autler-Townes (AT) splitting peaks, which correspond to the EIT peaks when the microwave field is applied. The arrows denote the positions of the $5P_{3/2}$(F′ = 4) – $57D_{3/2}$ and $5P_{3/2}$(F′ = 4) – $57D_{5/2}$ transitions without microwave field, respectively.

Results and discussion

Fig. 2 shows the microwave-assisted EIT spectra recorded by scanning the laser frequency while using different microwave frequencies. The EIT spectrum is obtained by sweeping the coupling laser frequency over the $5P_{3/2}$(F′ = 4) – $57D_{5/2}$ transition, whereas the probe laser frequency is in resonance with the $5S_{1/2}$(F = 3) – $5P_{3/2}$(F′ = 4) transition, and the arrows denote the positions of the $5P_{3/2}$(F′ = 4) – $57D_{3/2}$ and $5P_{3/2}$(F′ = 4) – $57D_{5/2}$ transitions. The powers of probe and the coupling lasers are 14 μW and 30 mW, respectively.

When a microwave field with a power of 6 dBm is applied to the atomic system, the transmission peaks of the $58P_{3/2}$ and $56F_{7/2}$ states can be observed as the frequency varies from 10.884 GHz to 12.804

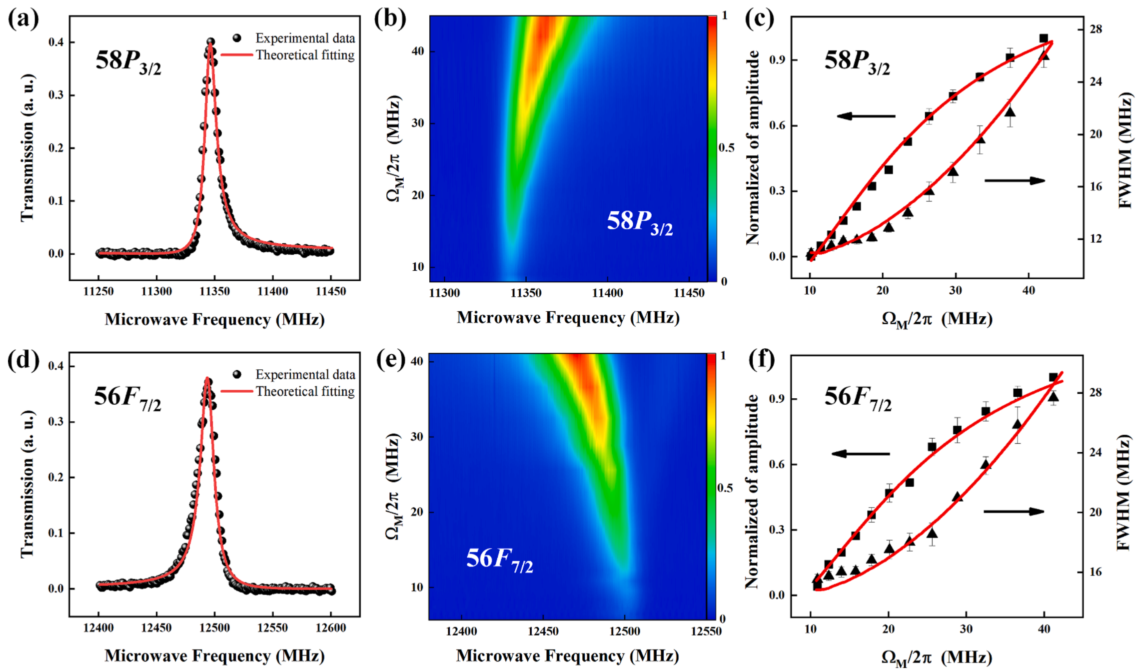

Fig. 3. Microwave-assisted EIT spectra versus the microwave frequency for (a) 58$P_{3/2}$ and (b) 56$F_{7/2}$ states. The black dots are the experimental results, and the red lines are the corresponding theoretical fits. (b) and (e) show the contour plots of the corresponding spectra as a function of the microwave field frequency with different Ω_M, respectively. Panels (c) and (f) show the dependence of the full width at half maximum (FWHM) (triangles) and the amplitude (squares) on Ω_M for 58$P_{3/2}$ and 56$F_{7/2}$ states, respectively. The red lines are the corresponding theoretical fits. (For interpretation of the references to colour in this figure legend, the reader is referred to the web version of this article.)

GHz. At the microwave frequency of 10.884 GHz, the transmission peak of the 58$P_{3/2}$ state appears. We can find that the peak's center position shifts with the microwave field frequency, and its theoretical trajectory is marked by black dashed line in Fig. 2 [31]. When the microwave field at the frequency of 11.364 GHz near resonate with the transition of 57$D_{5/2}$ − 58$P_{3/2}$, the EIT peak of the 57$D_{5/2}$ state is split into two peaks with equal heights (peak 1 and peak 2) [6–8]. As the increase of microwave field frequency, an interesting phenomenon appears. When the microwave field frequency is 11.604 GHz, the transmission peak for the 56$F_{7/2}$ state appears. The peak's center position also shifts with the microwave field frequency increases (blue dashed line in Fig. 2) and becomes obvious; however, the transmission peak of the 58$P_{3/2}$ state is small but clearly distinguishable when the frequency of microwave field is 12.084 GHz. It continues to decrease but can still be distinguished at the microwave frequency of 12.324 GHz. Therefore, we are able to resolve the transmission peaks of the 58$P_{3/2}$ and 56$F_{7/2}$ states from the spectra obtained when the detuning in the intermediate 57$D_{5/2}$ state less than a few hundred-megahertz.

The 57$D_{5/2}$ − 58$P_{3/2}$ and 56$F_{7/2}$ transition spectra are obtained by scanning the microwave frequency at a fixed frequency of the coupling laser. Fig. 3(a) shows the microwave-assisted EIT spectra versus the microwave field frequency for the 58$P_{3/2}$ state when the Rabi frequency of microwave field is $2\pi \times 14.3$ MHz. The frequency of the coupling laser is blue detuned 30 MHz to the 5$P_{3/2}$ – 57$D_{5/2}$ transition, which results in the detuning of the microwave field to be positive for the 58$P_{3/2}$ and negative for the 56$F_{7/2}$ states, respectively. Fig. 3(b) shows the microwave-assisted EIT spectra for the 58$P_{3/2}$ state as a function of the microwave field frequency with different Ω_M. As Ω_M increases, the strong transition between 57$D_{5/2}$ and 58$P_{3/2}$ states leads to the increase in the number of atoms in the 58$P_{3/2}$ state, so the amplitude of microwave-assisted EIT spectra increases. At the same time, the linewidth also is gradually widened due to the power broadening effect. We further extract the amplitude (squares) and FWHM (triangles) values and display them in Fig. 3(c). Fig. 3(d–f) show the case of the 56$F_{7/2}$ state. The normalization of amplitude in Fig. 3(c and f) is processed by

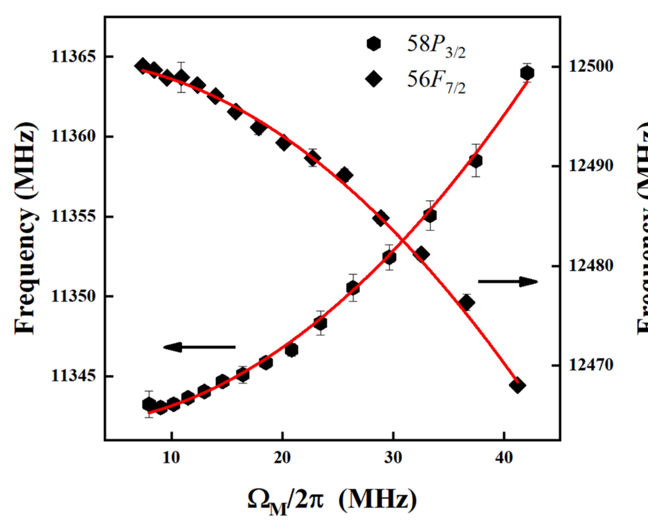

Fig. 4. The frequencies of the 57$D_{5/2}$ − 58$P_{3/2}$ and the 57$D_{5/2}$ − 56$F_{7/2}$ transitions as functions of Ω_M. The hexagons and rhombuses represent the experimental results. The red lines represent the fits to quadratic variations with Ω_M. (For interpretation of the references to colour in this figure legend, the reader is referred to the web version of this article.)

the maximum amplitude of microwave-assisted EIT spectra when Ω_M are $2\pi \times 44$ MHz and $2\pi \times 42.2$ MHz, respectively. For each measurement, we sweep the microwave frequency over the range of the resonance frequency, and the whole sweep process is repeated at least ten times. To quantitatively interpret the experimental results, a theoretical model is introduced. The susceptibility for a four-level system can be expressed as follows [32]:

Table 1
Transition frequencies of the n$D_{5/2}$ – (n+1)$P_{3/2}$ and n$D_{5/2}$ – (n-1)$F_{7/2}$ transitions (n = 51–57), including the experimental uncertainties in parentheses (units in MHz).

n	Corrected intervals (MHz)	
	n$D_{5/2}$-(n + 1)$P_{3/2}$	n$D_{5/2}$-(n-1)$F_{7/2}$
51	16028.692(87)	17546.568(70)
52	15094.847(67)	16530.136(17)
53	14232.140(62)	15592.839(88)
54	13432.920(84)	14722.367(36)
55	12693.552(29)	13918.792(23)
56	12006.073(38)	13170.197(22)
57	11368.621(65)	12473.974(69)

$$\chi_k \approx i\frac{3N_0\Gamma\lambda_p^3}{8\pi^2\left(\gamma_{12}-i(\Delta_p-\varepsilon\Delta_1)+\frac{\Omega_c^2\Omega_M^2}{16\Delta_c^2(\gamma_{14}-i(\Delta_p+\varepsilon\Delta_c+\Delta_M-\varepsilon\Delta_2))}\right)} \tag{1}$$

where λ_p is the wavelength of the probe laser, Γ is the decay rate, N_0 is the atomic density. γ_{ij} is the dephasing rate of the atomic coherence between states $|i\rangle$ and $|j\rangle$. Δ_p, Δ_c and Δ_M represent the detuning of the probe laser, the coupling laser, and the microwave field compared with their respective atomic resonance transitions, respectively. Ω_p, Ω_c and Ω_M represent the Rabi frequencies of the probe laser, the coupling laser, and the microwave field, respectively. ε is a coefficient, and $\varepsilon = -1$ for the (n+1)$P_{3/2}$ states and $\varepsilon = 1$ for the (n-1)$F_{7/2}$ states. Δ_1 is the frequency shift relative to Ω_c, $\Delta_1 = \frac{\Omega_c^2}{4\Delta_c}$, and Δ_2 is the frequency shift relative to Ω_M, $\Delta_2 = \frac{\Omega_M^2}{4\Delta_c}$. The theoretical fits are in good agreement with the experimental results, as indicated by the red lines in Fig. 3.

In addition, the center frequency of the microwave-assisted EIT spectrum shifts with Ω_M owing to the AC Stark shifts of the 58$P_{3/2}$ and 56$F_{7/2}$ states induced by the detuned microwave field. The direction of the AC Stark shift is determined by the microwave field detuning relative to the resonance frequency. Fig. 4 shows the shifts of the center frequency of the 57$D_{5/2}$ − 58$P_{3/2}$ transition (hexagons) and the 57$D_{5/2}$ − 56$F_{7/2}$ transition (rhombuses) as a function of Ω_M, which are also extracted from Fig. 3(b) and (e), respectively. The red lines represent the theoretical fits to quadratic variations with Ω_M. It can be seen that the center frequency of the 57$D_{5/2}$ − 58$P_{3/2}$ transition increases as the increase of Ω_M, whereas that of the 57$D_{5/2}$ − 56$F_{7/2}$ transition decreases with increasing Ω_M. And the transition frequency without microwave field is obtained by extrapolating the results to zero microwave field [27]. The fitting error is less than 0.4 MHz. Taking into account the frequency detuning of the microwave field caused by the detuned coupling laser, the corrected transition frequencies of the 57$D_{5/2}$ − 58$P_{3/2}$ and 56$F_{7/2}$ transitions are 11368.621(65) MHz and 12473.974 (69) MHz, respectively. Further, a series of atomic resonant transition frequencies of $nD_{5/2}$ – (n+1)$P_{3/2}$ and $nD_{5/2}$ – (n-1)$F_{7/2}$ transitions (n = 51–56) are measured by the same method. The resulting values are listed in Table 1, which are the averages of three measurements.

Table 2
Quantum defect constants δ_0 and δ_2 for the $P_{3/2}$ and $F_{7/2}$ − series of ^{85}Rb.

Reference	The transition process	δ_0	δ_2
$P_{3/2}$-series			
This work	5$S_{1/2}$-5$P_{3/2}$-$nD_{5/2}$-(n+1)$P_{3/2}$	2.64142(15)	0.295
2003, W. Li *et al.* [22]	5$S_{1/2}$-5$P_{3/2}$-$nS_{1/2}$-$nP_{3/2}$	2.6548849 (10)	0.2950(7)
2009, B. Sanguinetti *et al.* [15]	5$S_{1/2}$-5$P_{3/2}$-5$D_{5/2}$-$nP_{3/2}$	2.641352	0.4822
2019, M. Li *et al.* [19]	5$S_{1/2}$-$nP_{3/2}$	2.64115	0.295
$F_{7/2}$-series			
This work	5$S_{1/2}$-5$P_{3/2}$-$nD_{5/2}$-(n-1)$F_{7/2}$	0.016411(16)	−0.0784
2006, J. Han *et al.* [23]	5$S_{1/2}$-5$P_{3/2}$-(n+2)$D_{5/2}$-$nF_{7/2}$	0.0165437(7)	−0.086(7)
2010, L. Johnson *et al.* [16]	5$S_{1/2}$-5$P_{3/2}$-5$D_{5/2}$-n$F_{7/2}$	0.016473(14)	−0.0784 (7)

The primary factors that degrade the accuracy of the transition frequency measurements are frequency instabilities in the probe and coupling lasers, the location of the transmission peaks and the accuracy of the extrapolation fitting. We stabilized the frequency of the probe laser by SAS, which results in a frequency instability less than 600 kHz. And the frequency instability leads to a frequency shift of coupling laser by about 370 kHz The frequency of coupling laser is stabilized by the EIT spectrum, which produced a frequency shift less than 800 kHz. The spectral linewidth increases with the microwave field strength, which limits the spectral resolution and results a maximum fitting error of 0.5 MHz from multiple measurements. There is an uncertainty of up to 0.4 MHz in the extrapolation. Adding these errors in quadrature gives a total error of less than 1.2 MHz.

The frequency interval between two states of n and n' can be calculated by the Rydberg formula involving the quantum defects of the two levels [33]:

$$v_{nn'} = R^*c\left(\frac{1}{(n-\delta_n)^2} - \frac{1}{(n'-\delta_{n'})^2}\right) \tag{2}$$

where c = 2.99792458 × 10^{10} cm/s is the speed of light, R^* = 109736.605 cm^{-1} is the Rydberg constant, δ_n and $\delta_{n'}$ are the quantum defects of the initial ($nD_{5/2}$) and final states ((n+1)$P_{3/2}$ or (n-1)$F_{7/2}$),

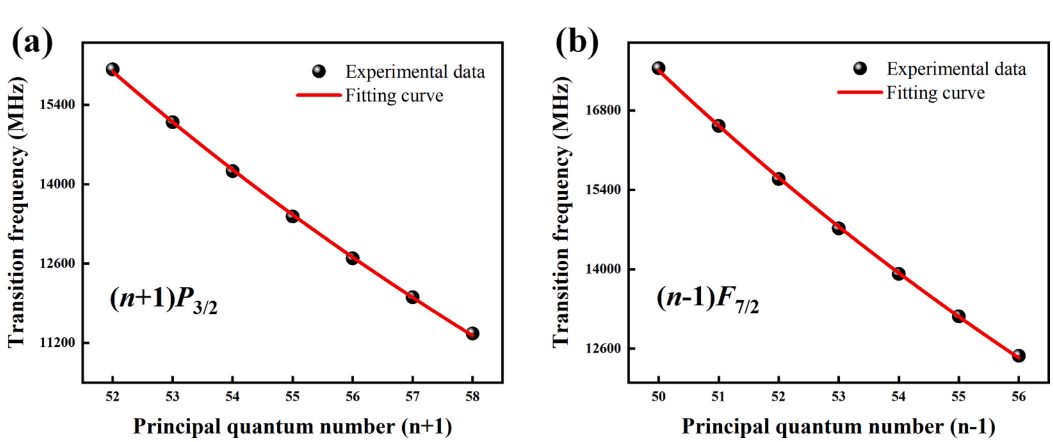

Fig. 5. Quantum defects obtained via fitting the frequencies of (a) the $nD_{5/2}$ – (n+1)$P_{3/2}$ and (b) the $nD_{5/2}$ – (n-1)$F_{7/2}$ transitions. The black dots indicate the experimental data, and the red solid lines are the theoretical fits to Eq. (2). (For interpretation of the references to colour in this figure legend, the reader is referred to the web version of this article.)

respectively. These quantum defects can be approximated by the modified Rydberg-Ritz coefficients when $n > 20$ [10,22,34,35]:

$$\delta_n \approx \delta_0 + \frac{\delta_2}{(n-\delta_0)^2} \tag{3}$$

where δ_0 and δ_2 are the quantum defect constants.

The quantum defects of the $(n+1)P_{3/2}$ or $(n\text{-}1)F_{7/2}$ states also can be extracted from the obtained frequency interval of the relational atomic energy levels. In order to verify the accuracy of the experimental data, $\delta_2 = 0.295$ for the $P_{3/2}$-series [22], and $\delta_2 = -0.0784$ for $F_{7/2}$-series are fixed [16], and the quantum defect constant δ_0 are extracted by fitting our experimental data. In our experiment, we adopt $\delta_0 = 1.34646572$, $\delta_2 = -0.59600$ [22] for the quantum defects of the $D_{5/2}$-series. The quantum defects of the $P_{3/2}$ and $F_{7/2}$-series are determined using the results obtained by fitting the transition frequencies (see the red lines in Fig. 5). The results are $\delta_0 = 2.64142(15)$ for $P_{3/2}$-series (with the fixed value $\delta_2 = 0.295$) and $\delta_0 = 0.016411(16)$ for $F_{7/2}$-series (with the fixed value $\delta_2 = -0.0784$) (see Table 2), the numbers in the parentheses are the standard error. The experimental results are consistent with the previous results for ^{85}Rb. Higher measurement accuracy of quantum defects can be achieved by measuring more transition frequencies over an extended range of principal quantum number n.

Conclusion

In conclusion, we determined the quantum defects of $P_{3/2}$ and $F_{7/2}$-series of ^{85}Rb via microwave-assisted EIT spectroscopy. The dependence of the Stark shifts of the corresponding Rydberg states on the Rabi frequency of microwave field are comprehensively studied both theoretically and experimentally. The resonant transition frequencies of $nD_{5/2}$ to $(n+1)P_{3/2}$ and $(n\text{-}1)F_{7/2}$ states ($n = 51$–57) are obtained by extrapolating the results to zero microwave field. The quantum defects, $\delta_0 = 2.64142$ (15) (with δ_2 fixed at 0.295) for $P_{3/2}$-series and $\delta_0 = 0.016411$ (16) (with δ_2 fixed at -0.0784) for $F_{7/2}$-series, are extracted by the modified Rydberg-Ritz formula with the obtained transition frequencies. This work provides an effective verification of the existing theory and promotes the extension the quantum simulation techniques of high-lying Rydberg states. Note that transferring the current experiment to cold atom samples will definitely lead to an improvement in measurement accuracy in future work.

CRediT authorship contribution statement

Shaohua Li: Investigation, Formal analysis, Data curation, Writing - original draft. **Jinpeng Yuan:** Conceptualization, Formal analysis, Project administration, Funding acquisition, Writing - review & editing. **Lirong Wang:** Formal analysis, Funding acquisition, Resources, Supervision, Writing - review & editing. **Liantuan Xiao:** Funding acquisition, Resources, Supervision. **Suotang Jia:** Funding acquisition, Resources, Supervision.

Declaration of Competing Interest

The authors declare that they have no known competing financial interests or personal relationships that could have appeared to influence the work reported in this paper.

Acknowledgements

This work was supported by the National Key R&D Program of China [Grant No. 2017YFA0304203]; the NSFC [Grants Nos. 61875112, 62075121, 91736209]; the Program for Sanjin Scholars of Shanxi Province; Key Research and Development Program of Shanxi Province for International Cooperation [Grant No. 201803D421034]; 1331KSC.

References

[1] Saffman M, Walker TG, Mølmer K. Quantum information with Rydberg atoms. Rev. Mod. Phys. 2010;82:2313. https://doi.org/10.1103/RevModPhys.82. 2313.
[2] Saffman M. Quantum computing with atomic qubits and Rydberg interactions: Progress and challenges. J. Phys. B: At. Mol. Opt. Phys. 2016;49(2):202001. https://doi.org/10.1088/0953-4075/49/20/202001.
[3] Peyronel T, Firstenberg O, Liang Q-Y, Hofferberth S, Gorshkov AV, Pohl T, et al. Quantum nonlinear optics with single photons enabled by strongly interacting atoms. Nature 2012;488(7409):57–60. https://doi.org/10.1038/nature11361.
[4] Liang Q-Y, Venkatramani AV, Cantu SH, Nicholson TL, Gullans MJ, Gorshkov AV, et al. Observation of three-photon bound states in a quantum nonlinear medium. Science 2018;359(6377):783–6. https://doi.org/10.1126/science:aao7293.
[5] Yuan J, Dong S, Wu C, Wang L, Xiao L, Jia S. Optically tunable grating in a V + Ξ configuration involving a Rydberg state. Opt. Express 2020;28(16):23820. https://doi.org/10.1364/OE.400618.
[6] Sedlacek JA, Schwettmann A, Kübler H, Löw R, Pfau T, Shaffer JP. Microwave electrometry with Rydberg atoms in a vapour cell using bright atomic resonances. Nat. Phys. 2012;8(11):819–24. https://doi.org/10.1038/nphys2423.
[7] Gordon JA, Holloway CL, Schwarzkopf A, Anderson DA, Miller S, Thaicharoen N, et al. Millimeter wave detection via Autler-Townes splitting in rubidium Rydberg atoms. Appl. Phys. Lett. 2014;105(2):024104. https://doi.org/10.1063/1.4890094.
[8] Anderson DA, Miller SA, Raithel G, Gordon JA, Butler ML, et al. Optical measurements of strong microwave fields with Rydberg atoms in a vapor cell. Phys. Rev. Applied 2016;5:034003. https://doi.org/10.1103/PhysRevApplied.5.034003.
[9] Jing M, Hu Y, Ma J, Zhang H, Zhang L, Xiao L, et al. Atomic superheterodyne receiver based on microwave-dressed Rydberg spectroscopy. Nat. Phys. 2020;16(9):911–5. https://doi.org/10.1038/s41567-020-0918-5.
[10] Lorenzen C-J, Niemax K. Quantum defects of the $n^2P_{1/2,3/2}$ levels in ^{39}K I and ^{85}Rb I. Phys. Scr. 1983;27:300. https://doi.org/10.1088/0031-8949/27/4/012.
[11] Safinya KA, Delpech JF, Gounand F, Sandner W, Gallagher TF. Resonant Rydberg-atom-Rydberg-atom collisions. Phys. Rev. Lett. 1981;47(6):405–8. https://doi.org/10.1103/PhysRevLett.47.405.
[12] Berl SJ, Sackett CA, Gallagher TF, Nunkaew J. Core polarizability of rubidium using spectroscopy of the ng to nh, ni Rydberg transitions. Phys. Rev. A 2020;102:062818. https://doi.org/10.1103/PhysRevA.102.062818.
[13] Yuan J, Dong S, Zhang H, Wu C, Wang L, Xiao L, et al. Efficient all-optical modulator based on a periodic dielectric atomic lattice. Opt. Express 2021;29(2):2712. https://doi.org/10.1364/OE.418000.
[14] Al-Awfi S, Bougouffa S. Quadrupole interaction of non-diffracting beams with two-level atoms. Results Phys. 2019;12:1357–62. https://doi.org/10.1016/j.rinp.2019.01.031.
[15] Sanguinetti B, Majeed HO, Jones ML, Varcoe BTH. Precision measurements of quantum defects in the $nP_{3/2}$ Rydberg states of ^{85}Rb. J. Phys. B: At. Mol. Opt. Phys. 2009;42(16):165004. https://doi.org/10.1088/0953-4075/42/16/165004.
[16] Johnson LAM, Majeed HO, Sanguinetti B, Becker Th, Varcoe BTH. Absolute frequency measurements of ^{85}Rb $nF_{7/2}$ Rydberg states using purely optical detection. New J. Phys. 2010;12(6):063028. https://doi.org/10.1088/1367-2630/12/6/063028.
[17] Li Y, Zaheeruddin S, Zhao D, Ma X, Yang J. Ionization spectroscopic measurement of nP Rydberg levels of ^{87}Rb cold atoms. J. Phys. Soc. Jpn. 2018;87(5):054301. https://doi.org/10.7566/JPSJ.87.054301.
[18] Li B, Li M, Jiang XJ, Qian J, Li XL, Liu L, et al. Optical spectroscopy of nP Rydberg states of ^{87}Rb atoms with a 297-nm ultraviolet laser. Phys. Rev. A 2019;99:042502. https://doi.org/10.1103/PhysRevA.99.042502.
[19] Li M, Li Bo, Jiang X, Qian J, Li X, Liu L. Measurement of ^{85}Rb nP-state transition frequencies via single-photon Rydberg excitation spectroscopy. J. Opt. Soc. Am. B 2019;36(7):1850. https://doi.org/10.1364/JOSAB.36.001850.
[20] Mack M, Karlewski F, Hattermann H, Hockh S, Jessen F, Cano D, et al. Measurement of absolute transition frequencies of ^{87}Rb to nS and nD Rydberg states by means of electromagnetically induced transparency. Phys. Rev. A 2011;83:052515. https://doi.org/10.1103/PhysRevA.83. 052515.
[21] Peper M, Helmrich F, Butscher J, Agner JA, Schmutz H, Merkt F, et al. Precision measurement of the ionization energy and quantum defects of ^{39}K I. Phys. Rev. A 2019;100:012501. https://doi.org/10.1103/PhysRevA. 100.012501.
[22] Li WH, Mourachko I, Noel MW, Gallagher TF. Millimeter-wave spectroscopy of cold Rb Rydberg atoms in a magneto-optical trap: Quantum defects of the ns, np, and nd series. Phys. Rev. A 2003;67:052502. https://doi.org/10.1103/PhysRevA.67.052502.
[23] Han JN, Jamil Y, Norum DVL, Tanner PJ, Gallagher TF. Rb nf quantum defects from millimeter-wave spectroscopy of cold ^{85}Rb Rydberg atoms. Phys. Rev. A 2006;74:054502. https://doi.org/10.1103/PhysRevA.74. 054502.
[24] Lee J, Nunkaew J, Gallagher TF. Microwave spectroscopy of the cold rubidium $(n+1)d_{5/2} \rightarrow ng$ and nh transitions. Phys. Rev. A 2016;94:022505. https://doi.org/10.1103/PhysRevA.94.022505.
[25] Tate DA, Gallagher TF. Microwave-optical two-photon excitation of Rydberg states. Phys. Rev. A 2018;97:033410. https://doi.org/10.1103/PhysRevA. 97.033410.
[26] Vogt T, Gross C, Gallagher TF, Li W. Microwave-assisted Rydberg electromagnetically induced transparency. Opt. Lett. 2018;43(8):1822. https://doi.org/10.1364/OL.43.001822.
[27] Dijck EA, Nuez Portela M, Grier AT, Jungmann K, Mohanty A, Valappol N, et al. Determination of transition frequencies in a single $^{138}Ba^{+}$ ion. Phys. Rev. A 2015;91:060501. https://doi.org/10.1103/PhysRevA. 91.060501.

[28] Tong D, Farooqi SM, Stanojevic J, Krishnan S, Zhang YP, Côté R, et al. Local blockade of Rydberg excitation in an ultracold gas. Phys. Rev. Lett. 2004;93(6). https://doi.org/10.1103/PhysRevLett.93.063001.
[29] Carollo RA, Carini JL, Eyler EE, Gould PL, et al. High-resolution spectroscopy of Rydberg molecular states of $^{85}Rb_2$ near the 5s+7p asymptote. Phys. Rev. A 2017; 95:042516. https://doi.org/10.1103/PhysRevA.95.042516.
[30] Gregoric VC, Bennett JJ, Gualtieri BR, Kannad A, Liu ZC, Rowley ZA, et al. Improving the state selectivity of field ionization with quantum control. Phys. Rev. A 2018;98(6). https://doi.org/10.1103/PhysRevA.98.063404.
[31] Kwak HM, Jeong T, Lee Y-S, Moon HS. Microwave-induced three-photon coherence of Rydberg atomic states. Opt. Commun. 2016;380:168–73. https://doi.org/10.1016/j.optcom.2016.06.004.
[32] Sandhya SN, Sharma KK. Atomic coherence effects in four-level systems: Doppler-free absorption within an electromagnetically-induced-transparency window. Phys. Rev. A 1997;55:2155. https://doi.org/10.1103/PhysRevA.55.2155.
[33] Gallagher TF. Rydberg Atoms, Cambridge Monographs on Atomic, Molecular and Chemical Physics. Cambridge University Press 1994. https://doi.org/10.1017/CBO9780511524530.
[34] Sansonetti CJ, Weber K-H. High-precision measurements of Doppler-free two-photon transitions in Rb: new values for proposed dye-laser reference wavelengths. J. Opt. Soc. Am. B 1985;2:1385. https://doi.org/10.1364/JOSAB. 2.001385.
[35] Deiglmayr J, Herburger H, Saßmannshausen H, Jansen P, Schmutz H, Merkt F. Precision measurement of the ionization energy of Cs I. Phys. Rev. A 2016;93: 013424. https://doi.org/10.1103/PhysRevA.93.013424.